PAPER

Check for updates

"Pea-pod-like" nitrogen-doped hollow porous carbon cathode hosts decorated with polar titanium dioxide nanocrystals as efficient polysulfide reservoirs for advanced lithium–sulfur batteries†

Weiqi Yao,[a] Chenjie Chu,[a] Weizhong Zheng,[a] Liang Zhan (ID) *[ab] and Yanli Wang*[a]

Lithium–sulfur (Li–S) batteries have been deemed as the best alternative for the new generation energy storage devices because of their high energy densities and low cost. Enhancing the sulfur utilization, decreasing the dissolution of lithium polysulfides (LiPSs) and improving the electrical conductivity of the cathodes have become the main challenges for the successful commercialization of Li–S batteries. In this paper, use of novel "pea-pod-like" nitrogen-doped hollow porous carbon cathode hosts decorated with polar titanium dioxide nanocrystals (rod-TiO$_2$@C) as high-efficiency polysulfide immobilizers for advanced Li–S batteries are reported. In this ingenious nanostructure, the hollow porous carbon can not only enhance the conductivity of the cathodes, but also effectively reserve sulfur species in its internal void space and the volume expansion upon lithiation can also be alleviated. More importantly, the well-dispersed polar TiO$_2$ nanocrystals can significantly suppress the dissolution of LiPSs and accelerate the redox reaction by strong chemical interactions. With a sulfur content of 65.4 wt%, the rod-TiO$_2$@C/S cathodes can deliver an extraordinary electrochemical performance in terms of high reversibility (1017 mA h g^{-1} after 200 cycles at 0.2C, 853 mA h g^{-1} after 500 cycles at 0.5C), superior rate capability (605 and 509 mA h g^{-1} at 8C and 10C, respectively) and excellent long-term cycle performance (728 mA h g^{-1} after 1500 cycles at 1C with an extremely low capacity loss of only 0.0196% each cycle, 604 mA h g^{-1} after 1500 cycles at 2C with a capacity loss of merely 0.0240% in each cycle). Furthermore, even under the high sulfur mass loading of 4.04 mg cm^{-2} and 3.89 mg cm^{-2}, the stable capacity (683 mA h g^{-1} after 300 cycles at 0.5C) and advanced rate performance (627 mA h g^{-1} at 2C) can be acquired, respectively.

1. Introduction

With the ever increasing requirement for massive new energy storage devices, the traditional Li-ion batteries (LIBs) have reached their energy density limitations and it has become difficult to satisfy the successful development of portable electronic devices, electric vehicles and hybrid electric vehicle.[1–5] Lithium–sulfur (Li–S) batteries have been considered as the most promising alternative for LIBs because the sulfur cathodes possess the advantages of high theoretical capacity (1672 mA h g^{-1}), energy density (2600 W h kg^{-1}), an ample amount of raw materials, inexpensive and environmental friendly.[6–12] However, the successful commercialization of Li–S batteries is still confronted with numerous obstacles, such as the insulating properties of sulfur (5 × 10^{-30} S cm^{-1}), discharge end products [lithium persulfide (Li$_2$S$_2$) and lithium sulfide (Li$_2$S)] and the dissoluble lithium polysulfides (LiPSs).[13,14] Meanwhile, the sulfur cathodes also suffer from serious volume changes (∼80%) upon lithiation. Furthermore, the serious "shuttle effect" which is caused by the dissolution of LiPSs into the electrolyte and the sluggish reaction kinetics from the conversion of polysulfide into insoluble Li$_2$S$_2$/Li$_2$S.[15,16] More importantly, the existence of challenges related to Li metal anodes also slows the application of Li–S batteries. Because of the high reactivity of fresh Li metal, it reacts with the electrolyte to instantly form the solid-electrolyte-interface (SEI) layer, which cannot accommodate large volume changes of the Li layer and continuously fractures during repeated cycling, thus leading to uninterrupted consumption of electrolyte, low

[a]State Key Laboratory of Chemical Engineering, Key Laboratory for Specially Functional Polymers and Related Technology of Ministry of Education, Shanghai Key Laboratory of Multiphase Materials Chemical Engineering, East China University of Science and Technology, Shanghai 200237, China. E-mail: zhanliang@ecust.edu.cn; ylwang@ecust.edu.cn; Fax: +86-21-6425-2914; Tel: +86-21-6425-2924

[b]CAS Key Laboratory of Carbon Materials, Institute of Coal Chemistry, Chinese Academy of Sciences, Taiyuan 030001, China

† Electronic supplementary information (ESI) available. See DOI: 10.1039/c8ta06288a

This journal is © The Royal Society of Chemistry 2018

J. Mater. Chem. A, 2018, 6, 18191–18205 | 18191

coulombic efficiency (CE) and serious corrosion of bulk Li. Additionally, Li metal protrusions can grow out of breaks in the SEI layer and the Li$^+$ may preferentially deposit onto these "naked" Li metal protrusions, which causes Li dendrite growth, which can penetrate separators, causing short circuits and other serious safety problems.[17,18] The previously mentioned problems inevitably lead to the sulfur utilization, inferior CE and poor cycle performance of Li–S batteries.[19,20]

Many strategies have been used to enhance the electrical conductivity of S cathodes and suppress the shuttle effect of LiPSs. Traditional carbonaceous nanomaterials [such as carbon nanotubes,[21] graphene,[22] micro–mesoporous carbon[23] and hollow carbon nanofibers/nanospheres[24]] have been extensively used for constructing all kinds of S/C cathodes. These carbon materials possess superb electrical conductivity and highly developed porosity, which can effectively guarantee the high sulfur loading and physically alleviate the dissolution of intermediate LiPSs. Although these S/C cathodes deliver high specific capacity at the beginning of several cycles, the capacity still decays rapidly during the subsequently cycles, and this phenomenon is mainly attributed to the relatively weak physical adsorption provided by the nonpolar carbon substrates which cannot effectively prevent the polar LiPSs dissolving into the organic electrolyte.[25–28] The real realized of Li–S batteries commercialization is also confronted with an enormous challenge.

Recently, all types of polar substances, such as the transition metal oxides [titanium dioxide (TiO$_2$),[29–33] manganese dioxide (MnO$_2$),[34–37] silicon dioxide (SiO$_2$),[38] iron(II,III) oxide (Fe$_3$O$_4$)[39] and niobium pentoxide (Nb$_2$O$_5$)],[40] sulfides [molybdenum disulfide (MoS$_2$),[41,42] tungsten disulfide (WS$_2$)[43] and niobium disulfide (NbS$_2$)[44]] and metal–organic frameworks[45–47] have been regarded as the best hosts because polar materials can form a stronger chemical interaction with LiPSs based on the strong Lewis acid–base interactions, which can efficiently restrain the shuttle effect and confine the sulfur species in the cathodes. However, the majority of polar substances have poor electrical conductivity, which is not favourable for fast electron transport and undoubtedly decreases the utilization of sulfur. Therefore, constructing hybrid nanostructures based on the synergistic effect between high conductivity porous carbon skeletons and polar materials should be the optimum scheme for enhancing the conductivity of sulfur cathodes, reserving sulfur species and providing a strong chemical affinity for blocking the dissolution of the intermediate LiPSs during the cycling process.

As is known, hollow carbon nanostructures are deemed to be one of the best candidates for sulfur host materials, because the sulfur nanoparticles are perfectly sealed into hollow porous carbon shells, which not only increases the electrical conductivity of the cathodes but also restricts the sulfur/polysulfides within their interior cavity.[24] The unusual "core–shell" nanostructure might also be responsible for the high sulfur loading content, alleviation of the volume expansion of sulfur upon lithiation and optimize the usage amount of electrolyte. Many studies have shown that heteroatom doping [such as nitrogen (N), sulfur (S) and boron (B)] of chemical modified carbon hosts can provide more defects and active sites, thus effectively

immobilizing LiPSs at electroactive sites via chemical interactions,[48–51] and theoretical calculations also indicate that pyridinic N can bind Li$_2$S/Li$_2$S$_2$ molecules, which may contribute to improving the cycle stability. In particular, TiO$_2$ has excellent adsorption ability as well as being toxic-free, which is beneficial for anchoring polysulfides. For example, Seh et al. showed that S–TiO$_2$ core–shell nanostructures could significantly enhance the long cycle stability of S cathodes.[29] However, the majority of as-synthesized TiO$_2$ hosts in current studies, because of its limited specific surface area and relatively small pore volume, have seriously limited higher sulfur loading and cannot physically confine the sulfur species.[52–57] Therefore, how to dramatically enhance the nanostructure stability, cycle stability, rate capability and long lifetime cathodes is still faced with numerous obstacles.

Taking the previously mentioned factors into consideration, in this research, novel "pea-pod-like" nitrogen-doped hollow porous carbon hosts decorated with polar TiO$_2$ nanocrystals (rod-TiO$_2$@C) have been successfully fabricated as efficient polysulfide immobilizers for fast and long lifetime Li–S batteries. Benefiting from the as-synthesized unusual one-dimensional (1-D) nanostructures, the rod-TiO$_2$@C host materials delivered several advantages for Li–S batteries. Firstly, the hollow "pea-pod-shaped" morphology cannot only buffer the volume change of sulfur upon lithiation, but also effectively physically encapsulate soluble Li$_x$S$_n$ within the structure. Secondly, the high specific area, large pore volume, co-existence with micro–mesoporous pore distribution could dramatically increase the loading amount of sulfur, and the 1-D inner void nanostructure provides a high aspect ratio and an efficient pathway for accelerating ion and electron transport. Thirdly, the N-doped chemically modified carbon hosts can immobilize LiPSs via chemical interactions. Finally, the polar TiO$_2$ acts as the significant electrocatalyst role for improving the redox reaction kinetics, which effectively form strong chemical interactions with the sulfur spices, decrease the dissolution of LiPSs and are beneficial for the high utilization of sulfur. As a consequence, the as-synthesized rod-TiO$_2$@C/S cathodes when used for Li–S batteries will enable high reversibility, outstanding cycle stability and excellent rate performance although under a high sulfur mass loading.

2. Experimental

2.1 Synthesis of 1-D ordered porous rod-SiO$_2$

The 1-D ordered porous rod-SiO$_2$ soft template was fabricated using cetyltrimethylammonium bromide (CTAB) and triblock copolymer Pluronic F-127 (EO$_{100}$PO$_{70}$EO$_{100}$) as the binary template, and ammonia catalyzed hydrolysis of tetraethyl orthosilicate (TEOS). In the typical experiment, 0.123 g of F-127 and 0.182 g of CTAB were dissolved in 3.5 mL and 12.5 mL of deionized water, respectively, and mixed ultrasonically until the solution became clear. Subsequently, 15 mL of ammonia solution (NH$_3$·H$_2$O, 2.5 wt%) was slowly added into previously mentioned mixture under stirring for 5 min, and then 0.6 mL of TEOS was added dropwise into the solution. After magnetic stirring for the next 3 min, the mixture was kept in an idle state

for 3 h at room temperature. The "milk-like" suspension obtained was centrifuged with ethanol, deionized water and then dried at 80 °C. The white power obtained was thermally treated at 550 °C for 6 h in air to remove the surfactant.

2.2 Synthesis of 1-D hollow porous rod-TiO$_2$@C and rod-C hosts

The nanocrystals of TiO$_2$ were deposited onto porous rod-SiO$_2$ using a kinetics controlled sol–gel method. Typically, a certain amount of the as-prepared porous rod-SiO$_2$ was initially dispersed in absolute ethanol using ultrasonic mixing for 20 min, 0.5 mL of NH$_3 \cdot$H$_2$O (28 wt%) was then added under stirring for 1 h at 45 °C. Tetrabutoxide titanate (TBOT) was diluted in ethanol and slowly injected into the mixture over more than 10 min, and then further stirred for 24 h at 45 °C. The intermediate products of rod-SiO$_2$@TiO$_2$ were collected using centrifugation with ethanol, then the wet centrifugation products were further dispersed in 100 mL of Tris-buffer solution (10 mM, pH = 8.5). Subsequently, 100 mg of dopamine (PDA) was added into mixture and stirred for one day at room temperature. After centrifugation with deionized water and drying, the rod-SiO$_2$@TiO$_2$@PDA powder obtained was carbonized at 800 °C in nitrogen (N$_2$) for 3 h. Finally, the thermally treated product, rod-SiO$_2$@TiO$_2$@C was etched from the silica in 2 M sodium hydroxide (NaOH) solution at 50 °C, resulting in the rod-TiO$_2$@C hosts. For comparison, the porous rod-SiO$_2$ was directly coated with PDA, after thermal treatment and etched off the SiO$_2$ sacrificial template to give the product, rod-C hosts.

2.3 Synthesis of 1-D rod-TiO$_2$@C/S and rod-C/S cathodes

The rod-TiO$_2$@C/S cathodes were fabricated using a classical melt-diffusion strategy. Typically, the as-synthesized rod-TiO$_2$@C and sublimed sulfur were simply homogenously mixed in an agate mortar with a weight ratio of 1 : 2 and encapsulated into a vacuum quartz tube. The mixture was then placed into a muffle furnace and treated at 155 °C for 10 h, followed by ramping the temperature to 300 °C for the next 2 h to guarantee that the sulfur had diffused completely into the pores. Similarly, the rod-C/S cathodes were prepared using the same method.

2.4 Preparation of lithium polysulfide solution and adsorption tests

The 3 mM lithium polysulfide (Li$_2$S$_6$) solution was prepared by dissolving a stoichiometric quantity of S and Li$_2$S (molar ratio of 5 : 1) containing a mixture of 1,2-dimethoxyethane (DME) and 1,3-dioxolane (DOL) solvent (1 : 1 v/v), and then vigorously stirred for 48 h in an argon filled glovebox. Subsequently, a 5 mg equivalent of rod-C or rod-TiO$_2$@C absorbents were added into 5 mL of Li$_2$S$_6$ solution. Digital images were taken 2 h after the start of the absorption experiment, and the rod-C-Li$_2$S$_6$ or rod-TiO$_2$@C-Li$_2$S$_6$ supernatant was diluted with DME/DOL solvent in a ratio of 1 : 20 to acquire a quantitative concentration for ultraviolet-visible (UV-vis) spectroscopy measurements using a spectrophotometer (PerkinElmer Lambda 950).

2.5 Computational methods

Quantum density functional theory (QDFT) methods were used to determine the binding energy (E_b) between the substrates and LiPSs, using:

$$E_b = E_{s+sub} - E_s - E_{sub}$$

where E_s, E_{sub} and E_{s+sub} correspond to the energy of LiPSs, substrate and LiPSs substrates, respectively. The first conformations of each molecule were obtained using a molecular mechanics method (Forcite module). The DFT calculation was made using the DMoL3 module of the Accelrys Material Studio software. The exchange correlation functional was obtained using a Perdew–Burke–Ernzerhof method. The one-body wave function is a figure amplified from the DNP basis set. The DFT semi-core pseudopotentials were used to calculate its core-electron interactions. The DFT-D correction (Grimme method) was utilized to determine the dispersion interactions. The solvation effect was determined using the COSMO model from the dielectric constant (6.18) in order to simulate the DOL/DME solvent. The adsorption of Li$_2$S$_6$ can be divided into two substrates: sp^2 carbon and TiO$_2$. Specifically, the sp^2 carbon was regarded as the infinite crystal, which can not only calculate in the periodic box with $a = b = 1.23$ nm, $c = 1.84$ nm, $\alpha = \beta = 90°$, and $g = 120°$ to imitate the real substrate, but also to eliminate the self-interaction of Li$_2$S$_6$. TiO$_2$ was divided into a double layered 1 nm × 1 nm (101 planes) segment to mimic the decoration particle. The structural optimization of QDFT was regarded to have converged when the energy change was below 6.275×10^{-3} kcal mol^{-1} and the force and displacement were lower than 0.0872 nN and 5×10^{-4} nm, respectively.

2.6 Material characterization

The microstructure of the materials were measured using field-emission scanning electron microscopy (SEM, FEI Nova Nano-SEM 450) and transmission electron microscopy (TEM, Jeol JEM-2100F), and the elemental distribution mapping was obtained using scanning TEM (STEM, Tecnai G2 F30) images. Thermogravimetric analysis (TG, TA Instruments Q600 analyzer) measurements were recorded in air and a N$_2$ atmosphere to evaluate the carbon and sulfur contents, respectively. The nitrogen adsorption–desorption measurements were recorded on a surface area and pore size analyzer (Quantachrome Instruments Quadrasorb SI) at 77 K. The Brunauer–Emmett–Teller (BET) method was used to calculate the specific surface area (S_{BET}), and the pore size distributions were originated from using the DFT method. X-ray diffraction (XRD, Rigaku D/Max-2550) was performed by using Cu Kα radiation ($\lambda = 0.15406$ nm) and 2θ ranging from 0.7–10° and 10–80° to measure the small and wide angles, respectively. The Raman spectrum were measured using optical spectroscopy (HORIBA Jobin Yvon Spex 1403) with an excitation laser wavelength of $\lambda = 514.5$ nm. The X-ray photoelectron spectroscopy (XPS, Axis UltraDLD) was performed on an instrument operated at 15 kV/10 mA to examine the surface chemical state.

2.7 Battery assembly and electrochemical tests

The working electrode was synthesized by mixing 80 wt% active materials (rod-TiO$_2$@C/S or rod-C/S), 10 wt% super C and 10 wt% polyvinylidene fluoride (binder) in *N*-methyl-2-pyrrolidone solvent. The homogeneous slurries were pasted onto aluminum foil and then dried. The electrode was divided into ϕ 12 mm (the electrode surface area = 1.1304 cm^2) disks and vacuum dried at 60 °C. Each electrode had a mass loading of sulfur of about 1.7–2 mg cm^{-2}. The CR2025 coin-type cell assembly was done in an Argon glovebox with lithium foil as anode. The electrolyte consisted of 1 M bis-(trifluoromethane) sulfonamide lithium (LiTFSI) containing a mixture of DME and DOL (1 : 1 v/v) containing an additive of 1 wt% of lithium nitrate. For each battery, the electrolyte usage was about 20 μL. The Celgard 2400 separator was used in the coin cell. The galvanostatic discharge/charge tests were carried out using a battery tester system (LAND CT2001A) with a cut-off voltage from 1.7–2.8 V. The cyclic voltammetry (CV) testing was recorded using an electrochemical workstation (Arbin BT2000) with a sweep rate of 0.1 mV s^{-1}. The electrochemical impedance spectroscopy (EIS, Gamry Instruments, PA, USA) was used in the frequency ranging from 0.01 to 10^5 Hz. All the electrochemical tests were conducted at 25 °C. The specific capacity value was calculated based on the sulfur content.

3. Results and discussion

Inspired by the extraordinary structure of the "green pea-pod" (Fig. 1a), this work aimed to construct this particular nanostructure as host materials for superior Li–S batteries. The detailed fabrication procedure of the rod-TiO$_2$@C/S cathodes are shown in Fig. 1b. First of all, the porous rod-SiO$_2$ soft template was synthesized using CTAB and F-127 as a binary template, under ammonia catalysed hydrolysis of TEOS.[58]

Secondly, TBOT was used for Ti precursor deposition of TiO$_2$ nanocrystals on the porous rod-SiO$_2$ using a kinetics controlled sol–gel method to give rod-SiO$_2$@TiO$_2$,[59] and the intermediate rod-SiO$_2$@TiO$_2$@PDA were acquired after coating with a thin shell of PDA (carbon source). After thermal treatment under a N$_2$ atmosphere, the rod-SiO$_2$@TiO$_2$@C was obtained. The "pea-pod-like" core–shell rod-TiO$_2$@C hosts were acquired after etching off the silica in NaOH solution. Eventually, commercial sulfur was incorporated into the rod-TiO$_2$@C hosts using a traditional melt-diffusion method to obtain the final product of rod-TiO$_2$@C/S cathodes. In contrast, the rod-SiO$_2$ was directly coated with a carbon shell to obtain the rod-C/S cathodes without addition of TiO$_2$.

In order to observe the microstructure of the samples, SEM and TEM measurements were initially carried out. As shown in the SEM images (Fig. S1, ESI†), it can be observed that the 1-D mono-dispersed "pea-pod-like" rod-SiO$_2$ has a smooth appearance. Also, the highly ordered porous nanostructure could also detected from the TEM images (Fig. S2, ESI†), with lateral dimension variation from 100 nm to 200 nm and a vertical size in the range of 200–400 nm. After the porous rod-SiO$_2$ was directly coated with carbon and etched off the silica, the SEM images (Fig. S3, ESI†) of the rod-C hosts obtained also showed its 1-D nanostructure. Because the PDA molecules can easily enter the highly porous rod-SiO$_2$ structure during the carbon-coating process, the TEM images (Fig. S4, ESI†) of rod-C gave the porous structure rather than the "core–shell" structure. After sulfur was infiltrated into the rod-C hosts using the traditional melt-impregnation method, the as-synthesized rod-C/S cathodes also maintained their original appearance (Fig. S5a–c, ESI†). The elemental mapping of rod-C/S (Fig S5d–f, ESI†) revealed the homogeneity of the C, S and N elements in the nanostructure. For comparison, after the formation of TiO$_2$ on the surface of the highly ordered porous rod-SiO$_2$ using *in*
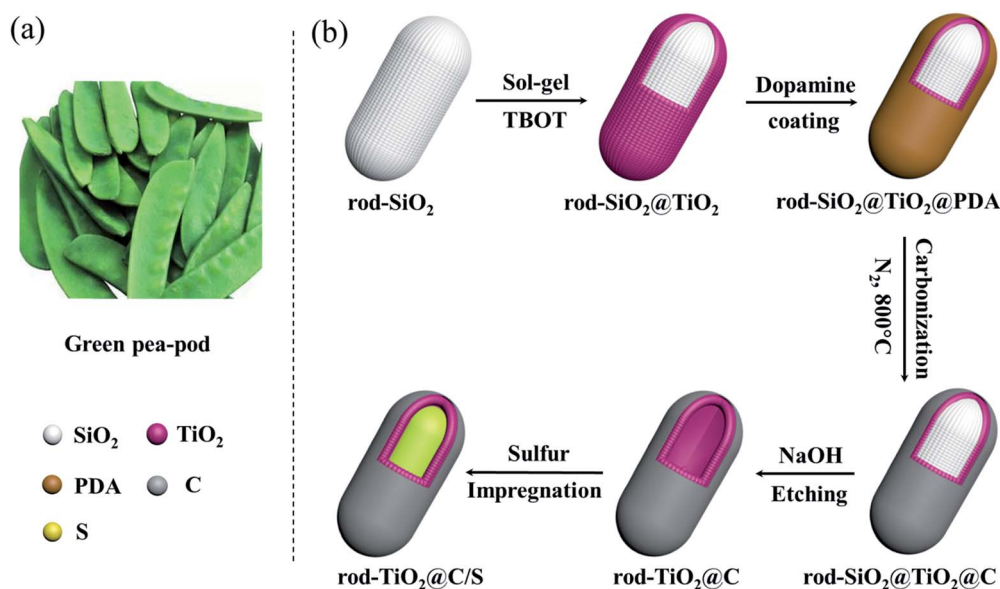

Fig. 1 (a) Digital photographs of "green pea pods". (b) The fabrication procedure diagram of the rod-TiO$_2$@C/S cathodes.

situ deposition, the surface of the rod-SiO_2@TiO_2 became rougher (Fig. S6a and b, ESI†), where the large quantities of small nanoplatelets can be clearly seen on the edge of the perpendicular towards the nanorod surface.[60] The rod-SiO_2@-TiO_2 exhibited no obvious microstructure distinct to rod-SiO_2, proving that the morphology was well preserved with few, if any, distortions. The elemental distribution (Fig. S6c–f, ESI†) of Si, O and Ti can be seen throughout the entire rod-SiO_2@TiO_2. Specifically, because the TiO_2 not only grows on the edge but also in the pores of rod-SiO_2 nanostructure, the Ti element mapping reveals the uniform distribution.[60] The intermediate product rod-SiO_2@TiO_2@C was also well preserved in its original "pea-pod-like" nanostructure after the carbon coating process (Fig. S7, ESI†). The rod-SiO_2@TiO_2@C (Fig. S8, ESI†) also showed uniform elemental distribution. After removal of the sacrifice layer of SiO_2, the rod-TiO_2@C also kept its nanorod appearance, as shown in the SEM images (Fig. 2a and b). The void interspace between the carbon layer and core can be easily detected in the TEM images (Fig. 2c), and the thickness of carbon shell was approximately 10 nm (Fig. 2d). Because the TiO_2 was initially deposited onto porous rod-SiO_2, this process may partially block the pores, for further carrying out the carbon coating process, PDA can grow on the edge or in the inner unblocked pores of the nanostructure. Strictly speaking, the unusual rod-TiO_2@C host materials should be regarded as the combination of outer hollow and inner partially porous nanostructure. In the high-resolution TEM (HRTEM) image (Fig. 2e), the representative lattice fringe distance was measured and was about 0.35 nm which corresponds to the *d*-spacing of

the (101) face of the anatase TiO_2.[61] The selected area electron diffraction (SAED) patterns (Fig. 2f) indicated the polycrystalline structure of TiO_2, and the diffraction rings from inside out can be inferred as being the (101), (004) and **(200) crystal faces of anatase TiO_2 phase, respectively.[62]

Commercial sulfur was loaded within the rod-TiO_2@C hosts using a traditional melt-diffusion method, and the SEM images obtained (Fig. 3a) revealed that the rod-TiO_2@C/S maintained their original "pea-pod-like" smooth appearance, indicating that no additional sulfur exists outside of the nanostructure. Its hollow structure can also be observed in the white rectangular region (Fig. 3b). The TEM image (Fig. 3c) and STEM image (Fig. 3d) show that the inner space for the rod-TiO_2@C/S became much darker after sulfur loading, indicating that the sulfur has been successfully accommodated and immobilized within the inner spaces. In order to further confirm the chemical constitution of the rod-TiO_2@C/S, an energy dispersive spectroscopy (EDS) was also used. As shown in Fig S9 (ESI),† the peak signals of C, S, Ti, O, N and copper (Cu) were detected in the EDS spectrum without observing any other impurity peaks. The corresponding elemental mapping (Fig. 3e–i) also revealed the homogeneous distributions of C, S, Ti, O, and N elements in the rod-TiO_2@C/S cathodes.

To confirm the porous nanostructure of the samples, the N_2 adsorption–desorption isotherms and pore characteristics were determined. As shown in Fig. S10 (ESI),† the rod-SiO_2 has an ultrahigh surface area (1986 m^2 g^{-1}) and pore volume (1.14 cm^3 g^{-1}), which may originate from the CTAB micelles constructed in the highly porous structure. The rod-TiO_2@C obtained
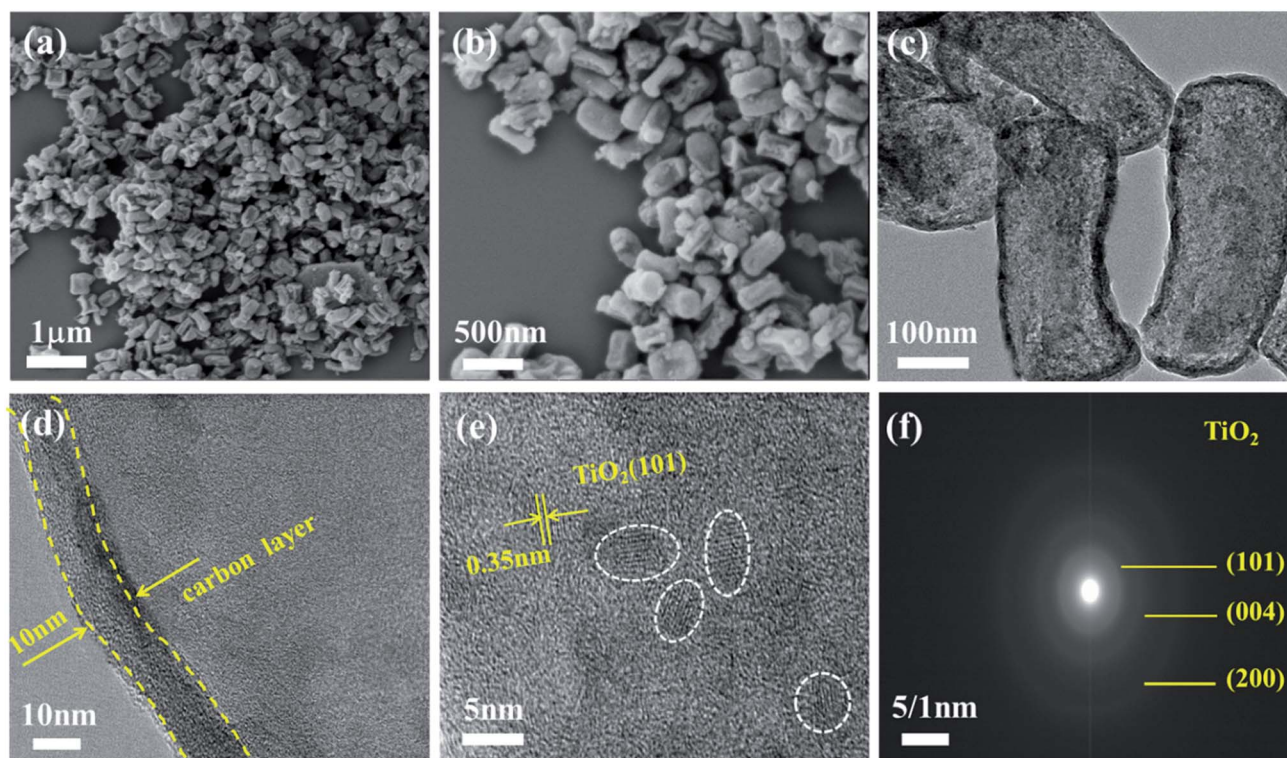

Fig. 2 SEM images (a and b), TEM images (c and d), HRTEM image (e) and its SAED pattern (f) of rod-TiO_2@C hosts.

This journal is © The Royal Society of Chemistry 2018

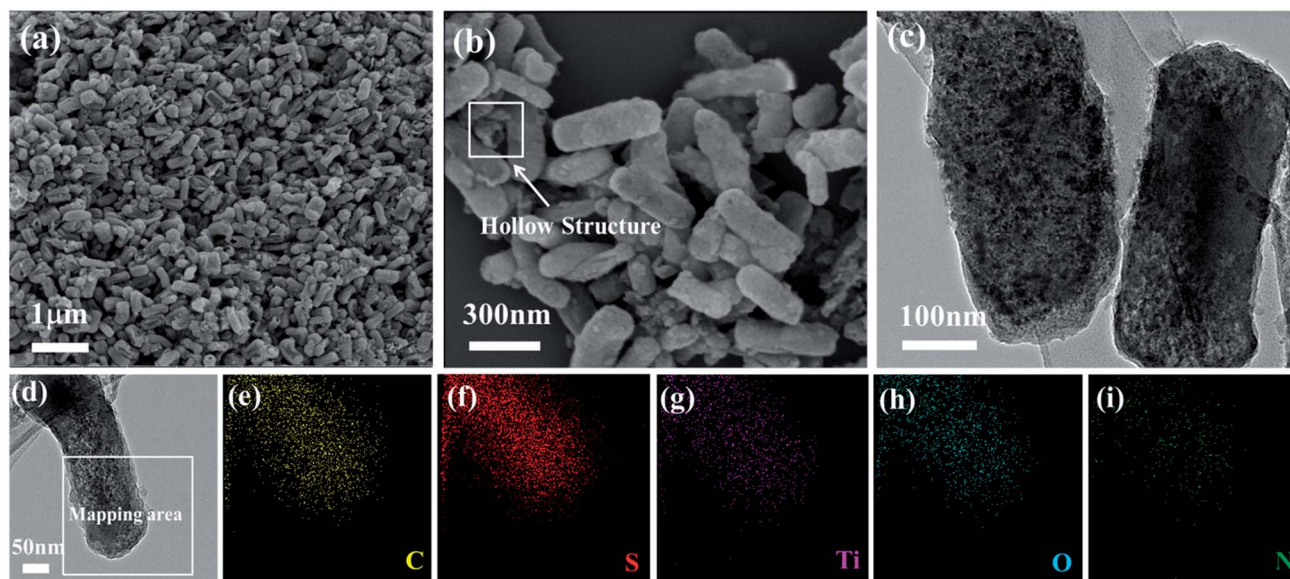*J. Mater. Chem. A*, 2018, **6**, 18191–18205 | **18195**

Fig. 3 SEM (a and b), TEM (c), STEM bright field images (d) and its elemental mapping images of carbon (e), sulfur (f), titanium (g), oxygen (h) and nitrogen (i) elements of rod-TiO$_2$@C/S cathodes.

showed a traditional IV adsorption isotherm with an obvious hysteresis loop at the relative pressure (P/P_0) of 0.5–1.0 (Fig. 4a), which caused a slight decrease in the surface area (757 m^2 g^{-1}) and pore volume (0.91 m^3 g^{-1}) compared with the rod-C [Fig. S11 (ESI),† 1077 m^2 g^{-1} and 1.01 cm^3 g^{-1}]. As shown in Fig. 4b, the pore size distribution of the rod-TiO$_2$@C exhibited obvious meso–microporous coexistence characteristics. The micropore and mesopore sizes were 1.56 and 3.54 nm,

respectively. The mesopores can be thought of as reservoirs for preserving sulfur and thus, enable high sulfur loading, and the micropores can be regarded as physical barriers for blocking the dissolution of LiPSs. Additionally, the highly developed porous structures which can not only facilitate the entry of sulfur into the porous channel, but also guarantee the transport and diffusion of ions. After sulfur impregnation into the pores, the specific area and pore volume of rod-TiO$_2$@C/S cathodes
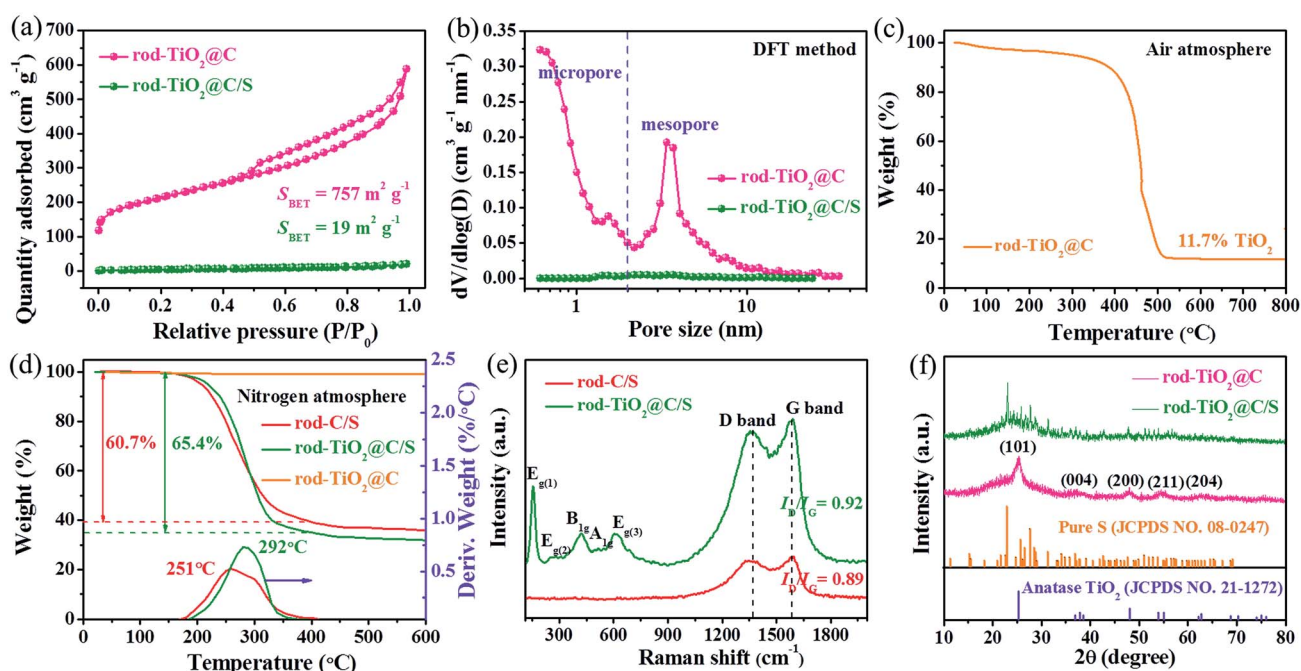

Fig. 4 Nitrogen adsorption–desorption isotherm (a) and the corresponding pore size distributions (b) of rod-TiO$_2$@C and rod-TiO$_2$@C/S. (c) TG curves of rod-TiO$_2$@C under air. (d) TG and DTG curves of rod-TiO$_2$@C, rod-C/S and rod-TiO$_2$@C/S under N$_2$. (e) Raman spectrum of rod-C/S and rod-TiO$_2$@C/S. (f) XRD patterns of rod-TiO$_2$@C and rod-TiO$_2$@C/S.

dramatically dropped to 19 m^2 g^{-1} and 0.03 cm^3 g^{-1}, respectively. The detailed pore characterization parameters for the samples are presented in Table S1 (ESI).† The TG analysis was also carried out under an air atmosphere, and the results for this are shown in Fig. S12 (ESI),† where the residual content in the rod-C was 0% at 800 °C, which shows that the SiO$_2$ has been completely etched off. Furthermore, the TiO$_2$ content in the rod-TiO$_2$@C (Fig. 4c) was estimated to be about 11.7 wt%. According to the results of the TG analysis under the N$_2$ atmosphere, the rod-C (Fig. S13, ESI†) and rod-TiO$_2$@C (Fig. 4d) apparently did not undergo weight loss up to 600 °C because of the stability of TiO$_2$ and porous carbon materials after the high temperature thermal treatment. Thus, the calculated sulfur contents in the rod-C/S and rod-TiO$_2$@C/S were 60.7 wt% and 65.4 wt%, respectively. It is worth noting that sulfur the evaporation temperature [derivative thermogravimetry (DTG) curves] for rod-TiO$_2$@C/S were obviously increased compared with those of the rod-C/S, which indicated that loading polar TiO$_2$ can enhance sulfur confinement.[40,41] In order to evaluate the degree of graphitization of the rod-C/S and rod-TiO$_2$@C/S, the Raman spectra were measured. As shown in Fig. 4e, The peaks located at 154, 201, 421, 515 and 610 cm^{-1} corresponded to the classical E$_{g(1)}$, E$_{g(2)}$, B$_{1g}$, A$_{1g}$ and E$_{g(3)}$ vibrational mode of the Ti–O bonds, respectively, which further proves the existence of TiO$_2$ in the rod-TiO$_2$@C/S.[62] Furthermore, both of the samples exhibit two obvious peaks located at 1368 and 1585 cm^{-1}, which were attributed to the vibrations of the D band (disordered carbon) and the G band (sp^2 ordered graphitic carbon), respectively. The relative peak intensity ratio value (I_D/I_G) demonstrated the extent of graphitization, defects and domain size of graphitization. The I_D/I_G ratio for rod-TiO$_2$@C/S (0.92) was a little higher than that of rod-C/S (0.89), showing that introduction of a certain amount of TiO$_2$ would increase the defects of the sample. Interestingly, the sulfur peak cannot be observed in the Raman spectrum after impregnation of sulfur into the hollow cavities of the micro–mesopore rod-TiO$_2$@C hosts. This verified that the majority of sulfur exists in the low molecular (S$_{2-4}$) species inside the narrow pores which cannot be detected by the Raman laser light, and this is beneficial for enhancing rate capability. Furthermore, the intensities of the TiO$_2$ peaks, D band and G band were increasing while the sulfur peak was diminishing in the rod-TiO$_2$@C/S, further demonstrating that the porous carbon was covering the majority of sulfur and therefore, blocked the sulfur signal of the Raman spectrum.[31,63,64] To confirm the crystallization properties of the samples, XRD was carried out. As shown in Fig. S14 (ESI),† the small angle XRD patterns suggested a highly ordered hexagonal mesostructure with a lattice space of 3.5 nm. The XRD pattern of rod-C (Fig. S15, ESI†) exhibited an obvious broad diffraction peak at a 2θ of ~26°, which was the (002) plane of amorphous carbon and it originated from PDA after the carbonization process, whereas the XRD pattern of rod-TiO$_2$@C (Fig. 4f) shows an additional five diffraction peaks at 25.3°, 37.7°, 47.9°, 54.5° and 63.1°, which were indexed to the (101), (004), (200), (211) and (004) planes of anatase TiO$_2$ (JCPDS no. 21-1272), respectively.[65] After impregnation of sulfur, the diffraction peak of TiO$_2$ in the rod-TiO$_2$@C/S became relatively weak, and the other strong diffraction peaks mainly come from orthorhombic sulfur (JCPDS no. 08-0247).

The XPS was further used to determine the bonding characteristics and surface chemical composition for rod-C/S (Fig. S16, ESI†) and rod-TiO$_2$@C/S (Fig. 5). Five peaks located

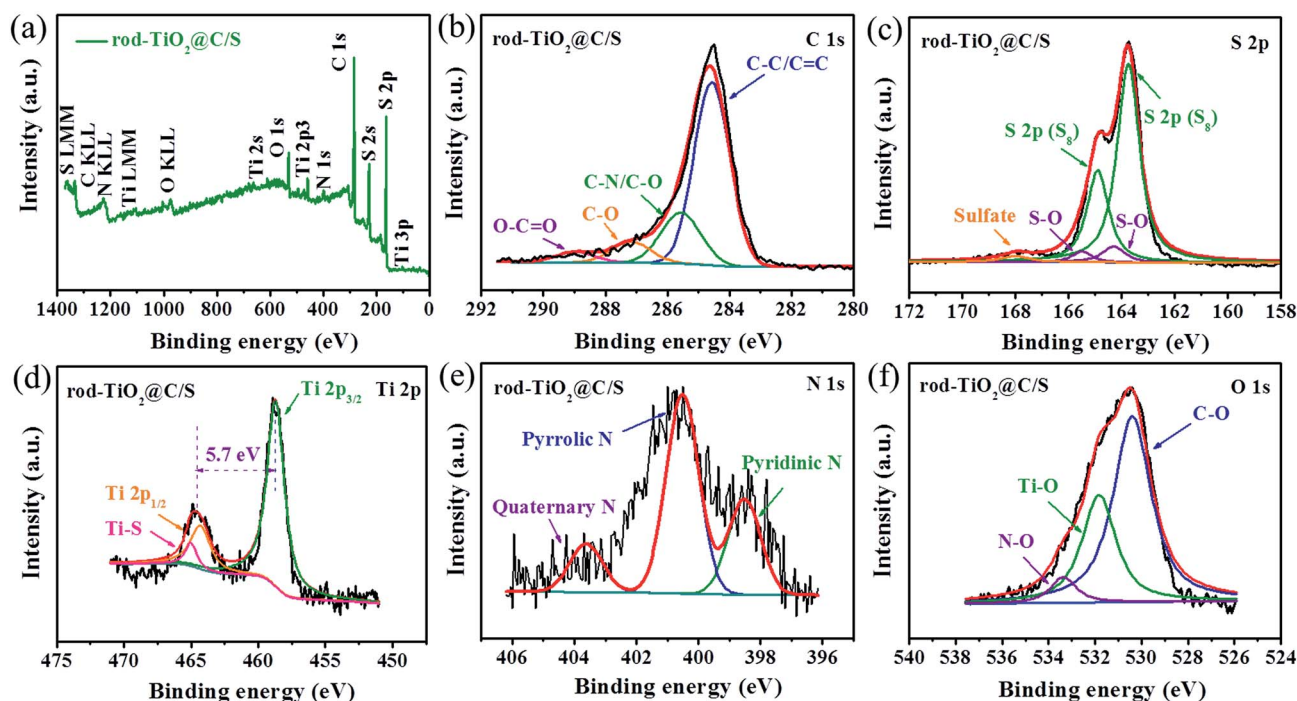Fig. 5 XPS full spectrum (a), the deconvoluted C 1s (b), S 2p (c), Ti 2p (d), N 1s (e) and O 1s (f) of rod-TiO$_2$@C/S.

This journal is © The Royal Society of Chemistry 2018

J. Mater. Chem. A, 2018, 6, 18191–18205 | 18197

at 164.0, 284.6, 401.5, 458.8 and 531.5 eV were observed in the overall spectra of rod-TiO_2@C/S (Fig. 5a), which were indexed to S 2p, C 1s, N 1s, Ti 2p[3] and O 1s, respectively. As shown in Fig. 5b, the high solution C 1s spectra can be divided into four bonds, C–C/C=C (284.6 eV), C–N/C–O (285.5 eV), C–O (287.2 eV) and O–C=O (289.0 eV), respectively. Notably, the C–N bond at 285.5 eV reveals that the N element has been completely doped in the carbon layer. The relative low peak intensity for C–O and O–C=O demonstrate that the majority of the oxygen containing functional groups in the carbon materials have been removed after the high temperature thermal treatment process. In the S 2p spectrum (Fig. 5c), two adjacent spin–orbit levels located at 164.7 eV and 163.8 eV were attributed to the S $2p_{1/2}$ and S $2p_{3/2}$ of the chemical bonds towards sulfur (S_8), respectively. The S–O bonds (165.5 eV and 164.3 eV) were also observed in the rod-TiO_2@C/S, which demonstrated the chemical interaction of sulfur with the amorphous carbon substrates.[66,67] Furthermore, the peak at 168.0 eV was consistent with sulfate species. The Ti 2p spectra (Fig. 5d) shows two predominant bonds at 458.7 eV and 464.4 eV, which can be indexed to Ti $2p_{3/2}$ and Ti $2p_{1/2}$, respectively. Its spin energy separation was 8.5 eV, which agreed well with the normal state of Ti^{4+} in the anatase TiO_2.[68] Also, the peak located at 464.8 eV should correspond to the Ti–S bonds, proving the existence of Ti–S interactions in the rod-TiO_2@C/S. More importantly, the Ti–S bonds reveal the chemical adsorption ability and the binding energy between TiO_2 and sulfur, which can effectively restrain the dissolution of the polysulfide intermediate through the Lewis acid–base interaction.[31] The high-solution N 1s spectra (Fig. 5e) was fitted to three bonds belonging to pyridinic N (398.5 eV), pyrrolic N (400.5 eV) and quaternary N (403.6 eV). The amount of nitrogen doped in the rod-TiO_2@C/S total content was 4.5 wt% based on the XPS analysis, it is considering that high conductive N-doped porous

carbon shows stronger chemical bonding with sulfur, guarantees direct and easy redox reactions of adsorbed polysulfides towards the conductive Lewis base "catalyst",[48] thus improving the sulfur utilization and cycle performance. Furthermore, the high solution O 1s spectra (Fig. 5f) was fitted to three bonds belonging to C–O (530.4 eV), Ti–O (531.8 eV) and N–O (533.4 eV), respectively.

The electrochemical performances of rod-TiO_2@C/S and rod-C/S cathodes as half-cells were investigated. Fig. 6a shows typical CV results, for rod-TiO_2@C/S and rod-C/S cathodes, of the first scan within the voltage window of 1.7–2.8 V with a sweep rate of 0.1 mV s^{-1}. The peaks of the rod-TiO_2@C/S cathodes deliver an identifiable positive shift in the cathodic reduction process and a negative shift in the anodic oxidation process compared with the rod-C/S cathodes, namely, the quasi-equilibrium potentials.[69] Furthermore, the rod-TiO_2@C/S cathodes show a higher peak intensity and large CV integral area compares with their counterpart rod-C/S, indicating its higher reactivity, enhanced polysulfide redox kinetics and significantly suppressed the electrochemical polarization. This phenomenon can be ascribed to the catalytic effect of TiO_2 on the oxidation/reduction of Li_2S/S. During the cathodic scans of the rod-TiO_2@C/S (Fig. 6b), two peaks (Peak I and II) located at 2.30 V and 2.04 V attributed to the typical multi-step reduction process of S_8 to the soluble long-chain polysulfides (Li_2S_x, $3 \leq x \leq 8$) at higher potential and generation of insoluble short-chain Li_2S_2/Li_2S at lower potential, respectively. Also, two adjacent peaks (Peak III and IV) in the anodic scan at around 2.35 V and 2.39 V originated from the converse oxidation process, (i.e., Li_2S_2/Li_2S to Li_2S_x, and then to S_8).[19] More importantly, the reduction and oxidation peaks remained almost constant in the subsequent cycles, showing the excellent electrochemical stability of the rod-TiO_2@C/S cathodes. The CV curves of the rod-C/S cathodes
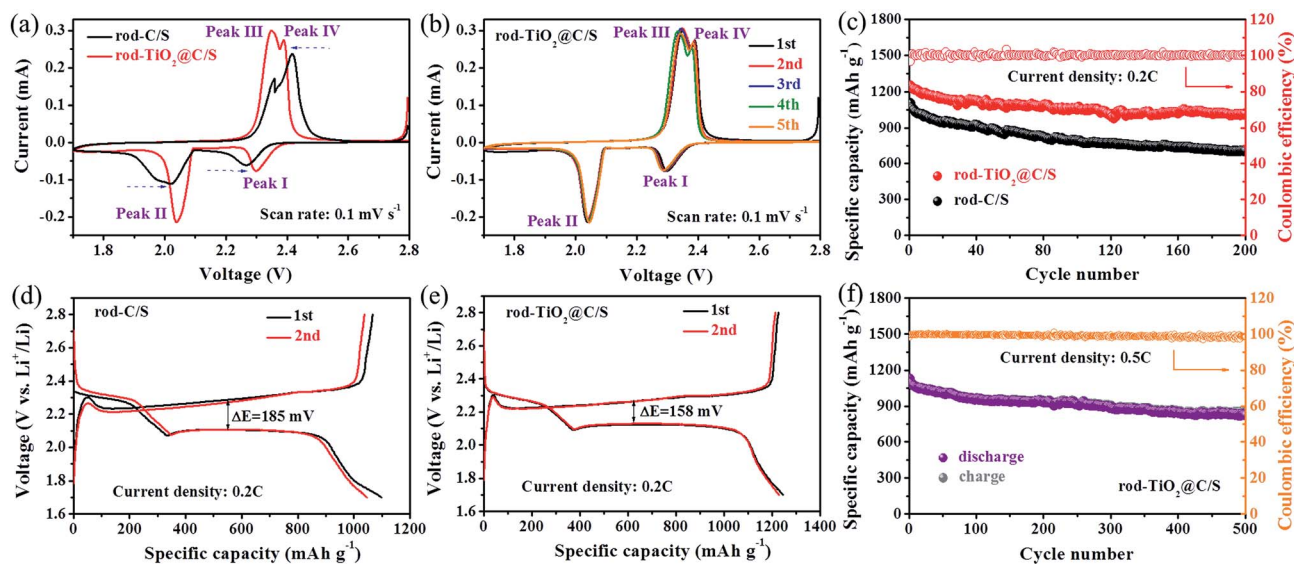

Fig. 6 (a) The comparison of representative CV curves at the first scan for rod-C/S and rod-TiO_2@C/S cathodes with a sweep rate of 0.1 mV s^{-1}. (b) CV curves for five cycles for rod-TiO_2@C/S cathodes with a sweep rate of 0.1 mV s^{-1}. (c) Cycle performance for rod-C/S and rod-TiO_2@C/S cathodes at the current density of 0.2C. Galvanostatic discharge–charge voltage profiles of rod-C/S (d) and rod-TiO_2@C/S (e) cathodes at the current density of 0.2C. (f) Cycle performance of rod-TiO_2@C/S cathodes at 0.5C.

18198 | J. Mater. Chem. A, 2018, 6, 18191–18205

This journal is © The Royal Society of Chemistry 2018

(Fig. S17, ESI†) show the obvious decreasing peak intensity, which demonstrated the existence of irreversible capacity loss. Fig. 6c shows the cycle performance of rod-C/S and rod-TiO$_2$@C/S cathodes at 0.2C (1C = 1675 mA h g^{-1}). The rod-TiO$_2$@C/S cathodes delivered a high initial discharge capacity of 1248 mA h g^{-1}, and the reversible specific capacity could be obtained as high as 1017 mA h g^{-1} after 200 cycles, with a high capacity retention of 81.5% and the coulombic efficiency maintained about 99%. For comparison, the rod-C/S cathodes exhibited a relatively lower first discharge specific capacity of 1099 mA h g^{-1}, with poor capacity retention of only 708 mA h g^{-1} after 200 cycles, proving the low utilization of

sulfur with serious dissolution of LiPSs into the electrolyte. As control experiments, rod-TiO$_2$@C/S cathodes with a higher sulfur loading [Fig. S18 (ESI),† 76.3%] were also synthesized to achieve the higher energy density. As shown in Fig. S19 (ESI),† the rod-TiO$_2$@C/S-76.3% cathodes also delivered a high initial discharge capacity of 1204 mA h g^{-1} under a current density of 0.2C, and acquired a slightly lower capacity of 958 mA h g^{-1} after 200 cycles. Because of the nanoscale distribution of sulfur particles, a hollow nanostructure and a porous carbon network, which provided the short diffusion path of electrons and lithium ions, thus guaranteed the efficient utilization of a high sulfur content.[70] Fig. 6d and e show the galvanostatic discharge/
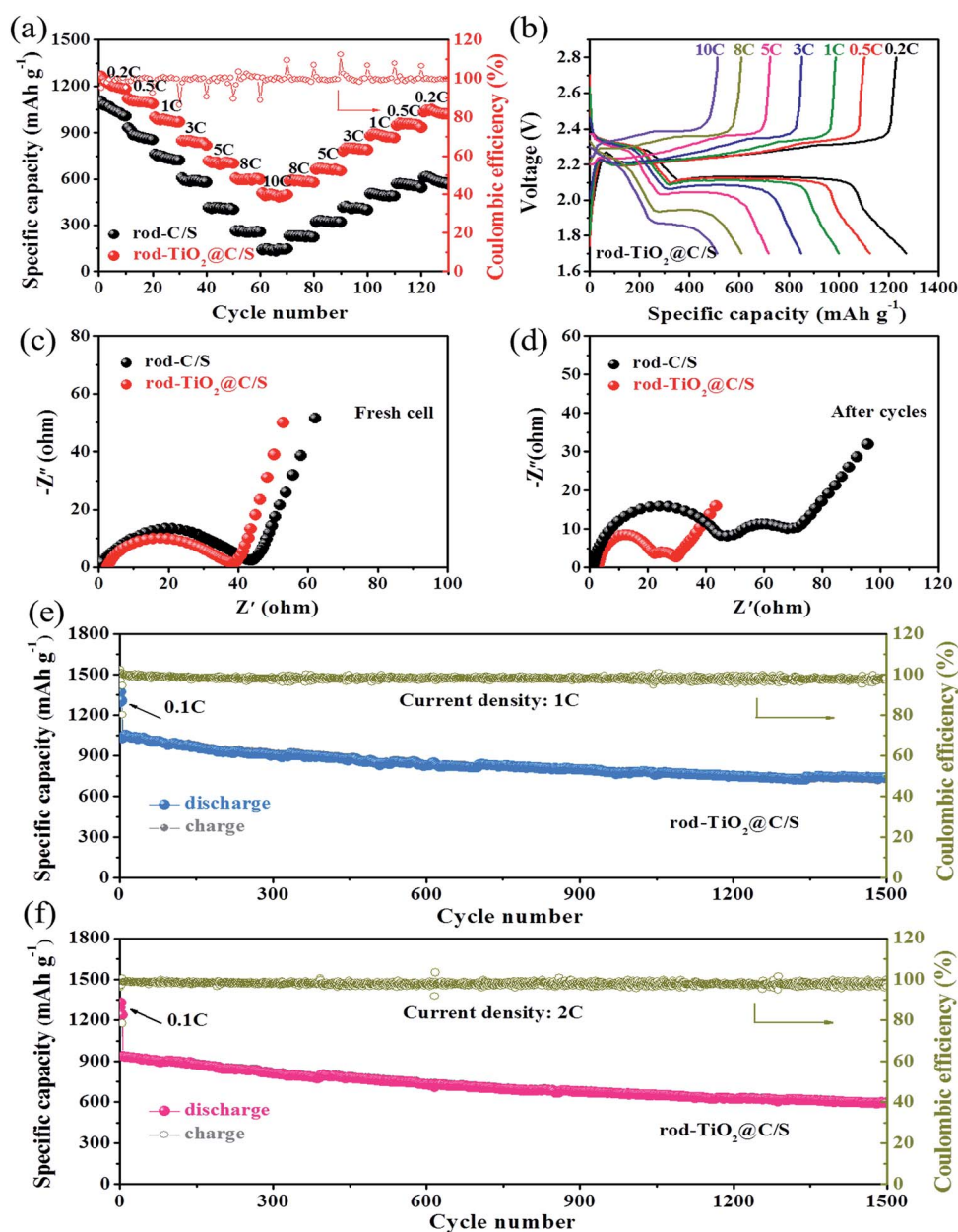

Fig. 7 (a) Rate performance of rod-C/S and rod-TiO$_2$@C/S cathodes under different current rates, (b) the corresponding discharge–charge curves of rod-TiO$_2$@C/S cathode for Li–S. Nyquist plots of rod-C/S and rod-TiO$_2$@C/S cathodes within the frequency range of 0.01–10^5 Hz before cycling (c) and after 200 cycles (d). (e) Long-term cycle performance of rod-TiO$_2$@C/S cathodes at 1C. (f) Long-term cycle performance of rod-TiO$_2$@C/S cathodes at 2C.

charge curves of rod-C/S and rod-TiO$_2$@C/S at 0.2C, respectively. The two representative plateaus located at about 2.3 V and 2.1 V can be distinctly detected in the discharge curves, which corresponded to the long-chain polysulfides (Li$_2$S$_x$, $3 \leq x \leq 8$) and short-chain Li$_2$S$_2$/Li$_2$S, respectively, and these were consistent with a sulfur multi-step in the CV curves. More importantly, the rod-TiO$_2$@C/S cathodes possessed a relatively low voltage operation polarization value of 158 mV between the discharge and charge plateaus, which was obviously lower than that of 185 mV for rod-C/S cathodes. The improved initial capacity and reductive polarization proved that TiO$_2$ was able to boost the electrochemical reaction kinetics of the cycling process. Impressively, rod-TiO$_2$@C/S cathodes (Fig. 6f) also delivered a high initial capacity of 1128 mA h g^{-1} at 0.5C. This can also keep a high reversibility of 853 mA h g^{-1} after 500 cycles, which corresponded to a high capacity retention of 75.6% and a capacity loss of merely 0.0488% each cycle.

The rate performance of rod-C/S and rod-TiO$_2$@C/S cathodes were further investigated under various rates from 0.2C to 10C (Fig. 7a). The rod-TiO$_2$@C/S cathodes acquired a high initial capacity of 1262 mA h g^{-1} at 0.2C, and accompanied with the current rates raised from 0.5C, 1C, 3C to 5C, it also delivered high capacities of 1118, 1001, 848 and 717 mA h g^{-1}, respectively. Also under the high current densities of 8C and 10C, high reversible capacities of 605 and 509 mA h g^{-1} were attained, respectively, indicating the excellent rate capability and fast reaction kinetics. As far as is known, such superior rate capabilities were almost never seen. When the current rates gradually returned step-by-step to 0.2C, the reversible capacity of 1107 mA h g^{-1} was recovered, suggesting the high reversibility of the rod-TiO$_2$@C/S cathodes. In contrast, the rod-C/S cathodes suffered from the rapid capacity decay at the same stepwise current rates. The corresponding discharge/charge profiles of rod-TiO$_2$@C/S cathodes under different current densities are also shown in Fig. 7b. It is worth noting that although under a high current density of 10C, the two representative voltage plateaus were also preserved except for some voltage drops because of the kinetic resistance. These results prove that embedded of TiO$_2$ nanocrystals can effective improve the kinetics of the LiPSs redox reactions and enhance the rate performance of the cathodes. To study the mechanism of improved cycle performance, electrochemical impedance spectroscopy (EIS) was also used to investigate the rod-C/S and rod-TiO$_2$@C/S cathodes before and after cycling. The relevant EIS equivalent circuits used to fit the values of the involved resistance are summarized in Fig. S20 (ESI).† The EIS spectrum for the fresh cells exhibits the depressed semicircle in a high-to-middle frequency region and a straight line in the low frequency area, which was related to the charge-transfer resistance (R_{ct}) and the Warburg resistance (Z_W) of the electrode, respectively.[71] It was interesting to find that the introduction of TiO$_2$ does not increase the impedance, as proved by the similar impedance values of rod-C/S and rod-TiO$_2$@C/S cathodes before cycling [Fig. 7c, Table S2 (ESI)†]. Compared with the fresh cells, the EIS spectra of the after cycling cells presented a fresh semicircle in the high frequency region, which corresponded to the formation of a SEI layer towards the insoluble Li$_2$S$_2$/Li$_2$S.

Obviously, the rod-TiO$_2$@C/S cathodes delivered a dramatic decrease of impedance after 200 cycles at 0.2C [Fig. 7d, Table S3 (ESI)†], because of containing TiO$_2$ nanocrystals which could effectively alleviate the dissolution of LiPSs and deposition of Li$_2$S/Li$_2$S$_2$ via stable chemical bonding interactions, and accelerated ion diffusion and kinetic reactions of the overall electrode. In contrast, the serious dissolution of LiPSs and poor electrochemical performance has occurred in the rod-C/S cathodes. To estimate the long-term cycle performance of rod-TiO$_2$@C/S cathodes, the fresh cell was first activated at 0.1C for five cycles, the rod-TiO$_2$@C/S cathodes exhibited a high initial capacity of 1031 mA h g^{-1} at 1C (Fig. 7e). Eventually, the rod-TiO$_2$@C/S cathodes delivered a high reversibility of 728 mA h g^{-1} after 1500 cycles, with a high capacity retention of 70.6% and a capacity loss of only 0.0196% each cycle. Similarly, the rod-TiO$_2$@C/S cathodes also acquired a high reversible capacity of 604 mA h g^{-1} after 1500 cycles at 2C (Fig. 7f), corresponding to the capacity decay of merely 0.0240% each cycle and the coulombic efficiency was maintained above 99%. Furthermore, from the visual observation of the DOL solvent, which contained the electrode after cycling (Fig. S21, ESI†), the rod-C/S cathodes exhibited much more "yellow" color, whereas the DOL solvent and corresponding separator color of the rod-TiO$_2$@C remained clear. This phenomenon indicated the physical entrapment of polar LiPSs in the rod-C/S, whereas the rod-TiO$_2$@C hosts had much stronger interaction with LiPSs to suppress the dissolution into the organic electrolyte. Additionally, the SEM images (Fig. S22, ESI†) of rod-C/S and rod-TiO$_2$@C/S cathodes after 200 cycles at 0.2C were carried out to explore the nanostructure stability. It was obvious that the rod-C/S cathodes had suffered serious mechanical instability with fragments of collapse, and the Li$_2$S$_2$/Li$_2$S was uncontrollable deposited on the surface of the electrode, and this further demonstrated that sulfur had left the host materials and dissolved into the electrolyte. In contrast, the rod-TiO$_2$@C/S cathodes almost keep the original "pea-pod-like" nanostructure with a smooth surface appearance, without apparent bulk Li$_2$S particles deposited onto the surface of the electrode. Therefore, it was concluded that nanocrystalline TiO$_2$ was an excellent polysulfide immobilizer, which can accelerate the chemical redox reactions of polysulfide, and reduce the occurrence of LiPSs dissolution.

In an effort to verify that the role of polar TiO$_2$ nanocrystals was to have a stronger adsorption ability towards lithium polysulfide, equal amount of the two host materials (5 mg rod-C or rod-TiO$_2$@C) were separately added into 3 mM Li$_2$S$_6$ in DOL/DME (1 : 1 v/v) solutions and mixed for 2 h. As shown in Fig. 8a, the digital image shows a visual difference between the contents of the three reagent bottles. Obviously, the color of the solution containing rod-TiO$_2$@C hosts became almost transparent, whereas the solvent color of the solution containing rod-C hosts only showed a slight variation of colour. This phenomenon suggested that rod-TiO$_2$@C had an excellent adsorption ability towards Li$_2$S$_6$ compared to the adsorption ability of rod-C. UV-vis spectroscopy (Fig. 8b) was also carried out to investigate the absorbance of the dilute solutions. The solution with rod-TiO$_2$@C delivered lower absorbance peak

18200 | *J. Mater. Chem. A*, 2018, **6**, 18191–18205

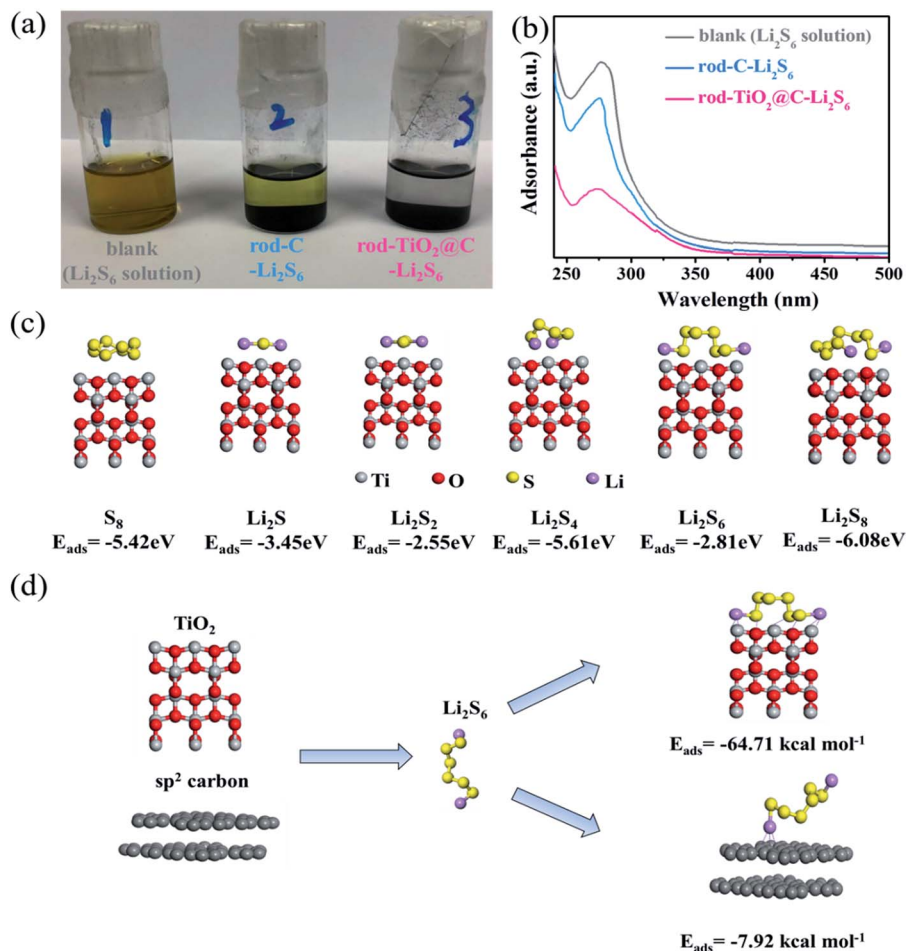This journal is © The Royal Society of Chemistry 2018

Fig. 8 (a) Digital photograph of polysulfide simulated, adsorption tests for rod-C/S and rod-TiO₂@C/S cathodes. (b) UV-vis adsorption spectra of lithium polysulfide (Li_2S_6) before and after addition of rod-C and rod-TiO₂@C. (c) Configurations and the binding energy between the TiO₂ nanocrystal (101) plane and sulfur species. (d) Binding geometric configurations and energies of a Li_2S_6 molecule with a two layer sp² carbon and TiO₂, which originated from *ab initio* calculations using the DFT model.

intensities than those containing rod-C or a blank (Li_2S_6 solution), indicating the different adsorption ability of polysulfide for these two host materials. To investigate the strong interaction between TiO₂ nanocrystals and sulfur species, theoretical simulations were further performed using DFT. Fig. S23 (ESI)† shows the optimization of a three-dimensional cluster structure of S_8 and Li_2S_x species, furthermore, the (101) planes of TiO₂ were chosen because they had the least surface energy and behaviour that was regarded as the most stable structure.[23] As illustrated in Fig. 8c, the binding energies calculation between TiO₂ nanocrystals with S_8, Li_2S, Li_2S_2, Li_2S_4, Li_2S_6 and Li_2S_8 species were: −5.42, −3.45, −2.55, −5.61, −2.81 and −6.06 eV, respectively, demonstrating the strong interaction effect between TiO₂ and sulfur species. According to the QDFT calculations (results shown in Fig. 8d), the binding energy between TiO₂ and Li_2S_6 (−64.71 kcal mol⁻¹) was more than eight times stronger than that of sp² carbon with Li_2S_6 (−7.92 kcal mol⁻¹). Fig. S24 (ESI)† further shows the geometric configurations and binding energies of a Li_2S_6 molecule with carbon host materials and TiO₂. In the Li_2S_6–TiO₂ system, the shortest distance between Li and Ti was 0.213 nm, which proves

the strong ionic bond of the Li and O atoms. The shortest distance between S and O was about 0.249 nm, showing the relative weak ionic bond and van der Waals force, which partially reinforced the interaction between Li_2S_6 and TiO₂. For comparison, a relatively long distance (0.256 nm) exists between the Li and C atom in the Li_2S_6–sp² carbon system. Additionally, there are several pairs of Li–Ti and Ti–S bonds contained in the Li_2S_6–TiO₂ system compared with just the one pairs which exist in the Li–C bond in the Li_2S_6–sp² carbon system. Therefore, the theoretical calculation further proves that TiO₂ can substantially enhance the adsorption ability for the host materials towards polysulfide, and this is expected to enhance the cycle performance of the sulfur cathodes.

Fig. 9a vividly illustrates the LiPSs diffusion mechanism of the electrodes before and after the discharge/charge process. Obviously, the liquid LiPSs can easily diffuse into electrolyte of rod-C/S cathodes because of its weak physical adsorption between polar LiPSs and nonpolar carbon, eventually leading to inferior electrochemical performance. In contrast, the strong chemical interaction between polar TiO₂ nanocrystals and polar LiPSs, the LiPSs intermediate was effectively
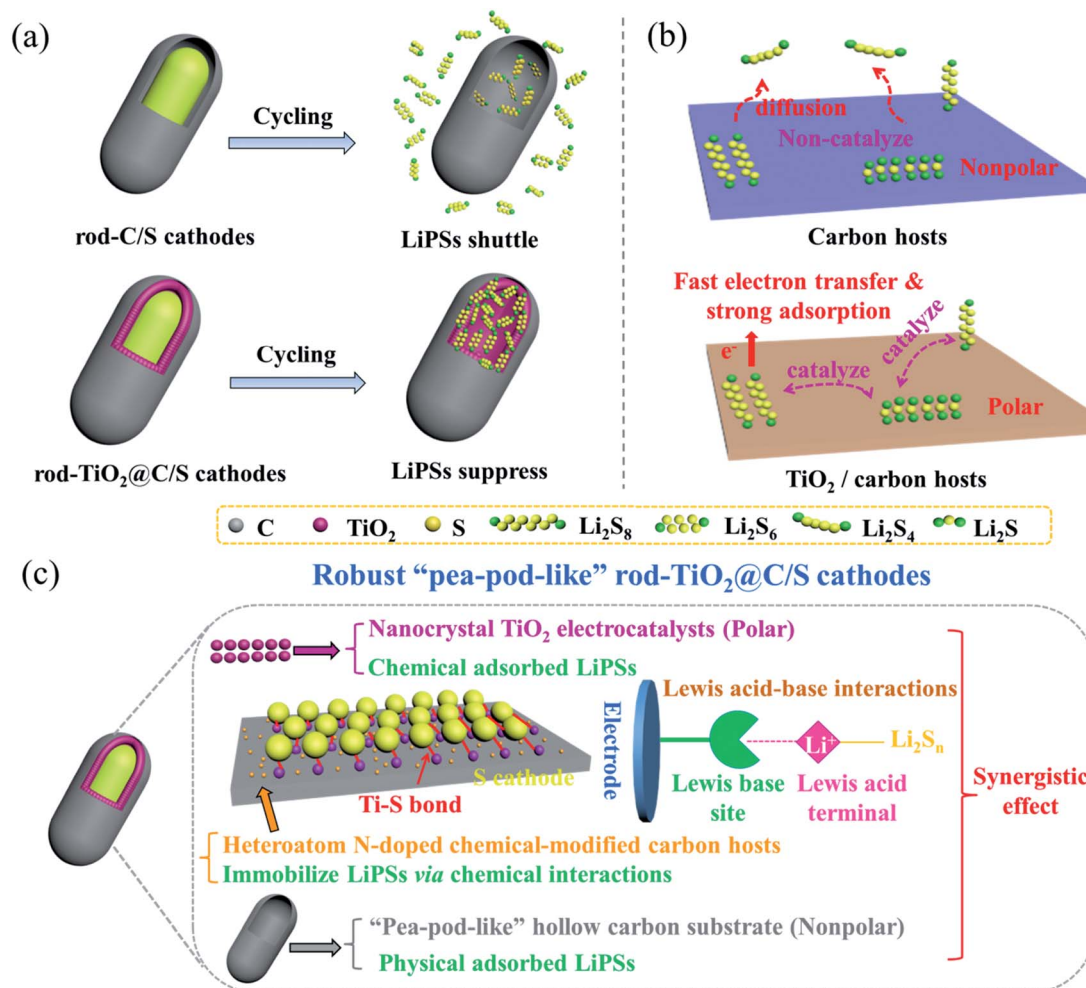
Fig. 9 (a) The LiPSs diffusion mechanism diagram of rod-C/S and rod-TiO$_2$@C/S cathodes before and after repeated cycling processes. (b) The comparison diagram of noncatalytic carbon host with catalytic TiO$_2$/carbon host diffusion of LiPSs. (c) Schematic illustration of the robust "pea-pod-like" rod-TiO$_2$@C/S cathodes with synergistic effect interaction.

restricted because of the rod-TiO$_2$@C/S cathodes. Consequently, the rod-TiO$_2$@C/S cathodes exhibited enhanced electrochemical reversibility and stability. Furthermore, the conversion reaction of LiPSs was slow, and the cycling process was kinetically sluggish because of the non-catalyst hosts (Fig. 9b). The soluble long-chain LiPSs can be efficiently converted to solid phase sulfur and Li$_2$S$_2$/Li$_2$S because of the accelerated polysulfide redox kinetics when the catalyst hosts were applied. The synergistic effect of TiO$_2$ and N-doped porous carbon (Fig. 9c) enabled the formation of robust cathode materials. First of all, the "pea-pod-like" hollow porous substrate can not only supply sufficient interspace of sulfur loading, physical confinement of LiPSs and alleviate volume expansion of sulfur upon lithiation, but can also construct an excellent conductive network for the cathodes. Secondly, the porous structure can homogeneously disperse sulfur and maintain a high contact surface area among active materials and electrolyte, provide a short channel for ion diffusion and transportation. Thirdly, TiO$_2$ acts as an electrocatalyst because of the Lewis acid–base interactions, which

can remarkably speed up LiPSs redox kinetics, particularly for the soluble Li$_2$S$_6$/Li$_2$S$_4$ transformation into the insoluble Li$_2$S$_2$/Li$_2$S.

With the expectation of improving the energy densities for Li–S batteries, a high sulfur mass loading and larger thickness electrode were prepared. As shown in Fig. 10a, with the increase of the areal mass loading, the rate capability decreased gradually, which could be ascribed to the decrease of the interfaces between the electrolyte and the thickness of the sulfur components, resulting in the enhancement of the charge transfer resistances.[13] Nevertheless, the rod-TiO$_2$@C/S cathodes still present outstanding rate capability although a high mass loading of 3.98 mg cm^{-2} is needed. The specific capacities of cathodes under 0.1C, 0.2C, 0.5C and 1C were 1109, 1047, 939 and 810 mA h g^{-1} (equivalent to areal capacities of 4.41, 4.17, 3.74, 3.22 mA h cm^{-2}), respectively. Excitingly, at the high current density of 2C, the high discharge capacity of 627 mA h g^{-1} (2.50 mA h cm^{-2}) can be obtained. When the current rates gradually recovers step-by-step to 0.1C, most of its original capacity could be attained, and this suggested that the
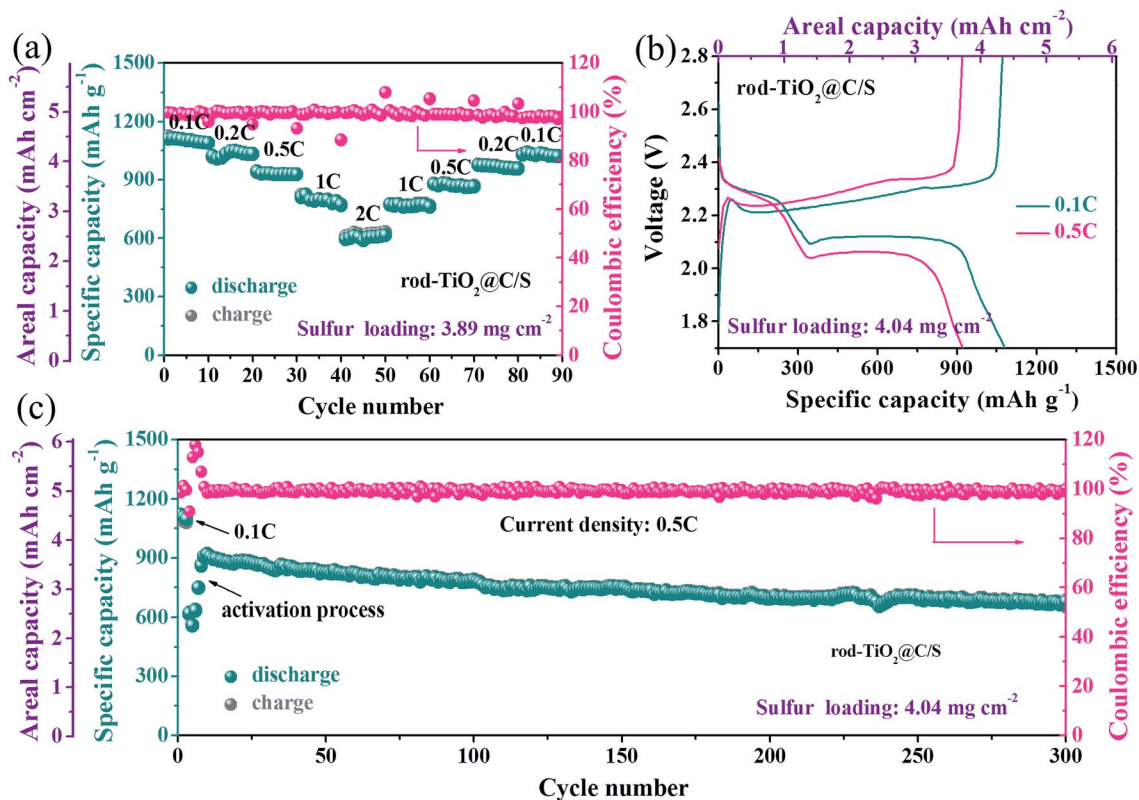
Fig. 10 (a) Rate performance of rod-TiO$_2$@C/S cathodes under 3.89 mg cm^{-2} sulfur mass loading. Galvanostatic discharge–charge voltage curves (b) and corresponding cycle performance (c) of rod-TiO$_2$@C/S cathodes at 0.5C under 4.04 mg cm^{-2} sulfur mass loading.

rod-TiO$_2$@C/S cathodes had high reversibility. The corresponding discharge/charge profiles of rod-TiO$_2$@C/S cathodes at different current densities are also shown in Fig. S25 (ESI).† Furthermore, as shown in Fig. 10b and c, the cathodes were further cycled at 0.5C (activated at 0.1C for three cycles), which delivered the highest initial specific capacity of 921 mA h g^{-1}, and eventually achieved an excellent specific capacity of 683 mA h g^{-1} after 300 cycles under a current density of 0.5C. It should be mentioned that the activation process (at the beginning of the 0.5C tests) can be attributed to the followed reasons.[45] On the one hand, sulfur approaching the outer surface of the nanostructure has more contact area with the carbon shell, and therefore reacts quicker than the sulfur sealed inside, nevertheless, the surface sulfur is more likely to get lost so causing the slight discharge capacity decreasing at the beginning of several cycles. On the other hand, for further cycles, the internal S became wetted by the electrolyte, producing more active sites towards the LiPSs, and the discharge capacity gradually increased and attained the peak value for several cycles. The outstanding cycle performance of the rod-TiO$_2$@C/S cathodes with a high sulfur mass loading can be ascribed to the strong chemical adsorption ability of TiO$_2$ and the high conductivity of the porous carbon shell, which promoted the ions' transportation and guaranteed the highly efficient sulfur utilization of the thick electrode. It is worth noting, that compared with previous reports in the literature other sulfur cathode materials utilizing metal oxide or metal

sulfide as an efficient polysulfide immobilizer for Li–S batteries, the synthesized rod-TiO$_2$@C/S cathodes described in this paper, deliver much better or at least comparable cycle stability (Table S4, ESI†) and rate performance (Table S5, ESI†).

4. Conclusion

In summary, an innovative architectural design combining well-dispersed polar TiO$_2$ nanocrystals and micro–mesoporous carbon nanomaterials as highly efficient sulfur host materials for future use in advanced Li–S batteries were designed and fabricated. The unique structure benefits from the synergistic effect between physical restriction and chemical interactions of the rod-TiO$_2$@C hosts. In detail, the hollow porous carbon nanostructure can physically confine LiPSs, and buffers the volume changes of sulfur upon lithiation, improves the electronic conductivity of the electrodes and facilitates electron and ion transportation during the cycling process. The experimental and theoretical calculations show that nanocrystalline TiO$_2$ is an excellent polysulfide immobilizer, which acts as electro-catalyst and accelerates the chemical redox reactions of poly-sulfide, reducing the dissolution of polysulfide and the shuttle effect. Because of the ingenious design, the rod-TiO$_2$@C/S cathodes obtained with 65.4% sulfur content delivered high reversibility (1017 mA h g^{-1} after 200 cycles at 0.2C, 853 mA h g^{-1} after 500 cycles at 0.5C), superior rate performance (605 mA h g^{-1} at 8C and 509 mA h g^{-1} at 10C) and

This journal is © The Royal Society of Chemistry 2018

J. Mater. Chem. A, 2018, **6**, 18191–18205 | **18203**

excellent long-term cycling performance (728 mA h g^{-1} after 1500 cycles at 1C with capacity loss merely 0.0196% for each cycle, 604 mA h g^{-1} after 1500 cycles at 2C and capacity decay of only 0.0240% per cycle). Remarkably, even under a high sulfur mass loading of 3.89 and 4.04 mg cm^{-2}, the superior rate capability (627 mA h g^{-1} at 2C) and excellent cycling performance (683 mA h g^{-1} after 300 cycles at 0.5C) can be acquired. This work provides a novel and feasible route for establishing cathode materials for future use as high rate and long lifetime Li–S batteries.

Conflicts of interest

There are no conflicts of interest to declare.

Acknowledgements

References

1 W. Yao, J. Chen, L. Zhan, Y. Wang and S. Yang, *ACS Appl. Mater. Interfaces*, 2017, **9**, 39371–39379.

2 Q. Liu, W. Yao, L. Zhan, Y. Wang and Y. Zhu, *Electrochim. Acta*, 2018, **261**, 35–41.

3 J. Leng, H. Mei, L. Zhan, Y. Wang, S. Yang and Y. Song, *Electrochim. Acta*, 2017, **231**, 732–738.

4 H. Wang, Y. Wei, J. Wang and D. Long, *Electrochim. Acta*, 2018, **269**, 724–732.

5 W. Yao, Y. Cui, L. Zhan, F. Chen, Y. Zhang, Y. Wang and S. Yan, *Appl. Surf. Sci.*, 2017, **425**, 614–621.

6 Y. Zhong, X. Xia, S. Deng, J. Zhan, R. Fang, Y. Xia, X. Wang, Q. Zhang and J. Tu, *Adv. Energy Mater.*, 2017, **8**, 1701110.

7 H. Peng, Z. Zhang, J. Huang, G. Zhang, J. Xie, W. Xu, j. Shi, X. Chen, X. Cheng and Q. Zhang, *Adv. Mater.*, 2016, **28**, 9551–9558.

8 C. Tang, Q. Zhang, M. Zhao, J. Huang, X. Cheng, G. Tian, H. Peng and F. Wei, *Adv. Mater.*, 2014, **26**, 6100–6105.

9 G. Hao, C. Tang, E. Zhang, P. Zhai, J. Yin, W. Zhu, Q. Zhang and S. Kaskel, *Adv. Mater.*, 2017, **29**, 1702829.

10 Z. Li, H. Wu and X. Lou, *Energy Environ. Sci.*, 2016, **9**, 3061–3070.

11 X. Wang, X. Bi, S. Wang, Y. Zhang, H. Du and J. Lu, *ACS Appl. Mater. Interfaces*, 2018, **10**, 16552–16560.

12 J. Zhang, Z. Li, Y. Chen, S. Gao and X. Lou, *Angew. Chem., Int. Ed.*, 2018, **57**, 1–6.

13 H. Peng, J. Huang, X. Cheng and Q. Zhang, *Adv. Energy Mater.*, 2017, **7**, 1700260.

14 L. Ma, R. Chen, G. Zhu, Y. Hu, Y. Wang, T. Chen, J. Lu and Z. Jin, *ACS Nano*, 2017, **11**, 7274–7283.

15 L. Ma, W. Zhang, L. Wang, Y. Hu, G. Zhu, Y. Wang, R. Chen, T. Chen, Z. Tie, J. Liu and Z. Jin, *ACS Nano*, 2018, **12**, 4868–4876.

16 L. Ma, H. Yuan, W. Zhang, G. Zhu, Y. Wang, Y. Hu, P. Zhao, R. T. Chen, J. Liu, Z. Hu and Z. Jin, *Nano Lett.*, 2017, **17**, 7839–7846.

17 G. Li, Y. Gao, X. He, Q. Huang, S. Chen, S. Kim and D. Wang, *Nat. Commun.*, 2017, **8**, 850.

18 G. Li, Q. Huang, X. He, Y. Gao, D. Wang, S. Kim and D. Wang, *ACS Nano*, 2018, **12**, 1500–1507.

19 F. Pei, L. Lin, D. Ou, Z. Zheng, S. Mo, X. Fang and N. Zheng, *Nat. Commun.*, 2017, **8**, 482.

20 J. Zhang, H. Hu, Z. Li and X. Lou, *Angew. Chem., Int. Ed.*, 2016, **55**, 3982–3986.

21 D. Su, M. Cortie and G. Wang, *Adv. Energy Mater.*, 2017, **7**, 1602014.

22 M. Yu, J. Ma, H. Song, A. Wang, F. Tian, Y. Wang, H. Qiu and R. Wang, *Energy Environ. Sci.*, 2016, **9**, 1495–1503.

23 S. Wu, Y. Wang, S. Na, C. Chen, T. Yu, H. Wang and H. Zang, *J. Mater. Chem. A*, 2017, **5**, 17352–17359.

24 W. Zhou, C. Wang, Q. Zhang, H. Abruña, Y. He, J. Wang, S. Mao and X. Xiao, *Adv. Energy Mater.*, 2015, **5**, 1401752.

25 W. Xue, Q. Yan, G. Xu, L. Suo, Y. Chen, C. Wang and J. Li, *Nano Energy*, 2017, **38**, 12–18.

26 H. Xu and A. Manthiram, *Nano Energy*, 2017, **33**, 124–129.

27 T. Chen, L. Ma, B. Cheng, R. Chen, Y. Hu, G. Zhu, Y. Wang, J. Liang, Z. Tie, J. Liu and Z. Jin, *Nano Energy*, 2017, **38**, 239–248.

28 J. Pu, Z. Shen, J. Zheng, W. Wu, C. Zhu, Q. Zhou, H. Zhang and F. Pan, *Nano energy*, 2017, **37**, 7–14.

29 Z. Seh, W. Li, J. Cha, G. Zheng, Y. Yang, M. McDowell, P. Shu and Y. Cui, *Nat. Commun.*, 2013, **4**, 1331.

30 Z. Li, J. Zhang, B. Guan, D. Wang, L. Liu and X. Lou, *Nat. Commun.*, 2016, **7**, 13065.

31 M. Fang, Z. Chen, Y. Liu, J. Quan, C. Yang, L. Zhu, Q. Xu and Q. Xu, *J. Mater. Chem. A*, 2018, **6**, 1630–1638.

32 T. Zhou, W. Lv, J. Li, G. Zhou, Y. Zhao, S. Fan, B. Liu, B. Li, F. Kang and Q. Yang, *Energy Environ. Sci.*, 2017, **10**, 1694–1703.

33 Z. Li, B. Guan, J. Zhang and X. Lou, *Joule*, 2017, **1**, 576–587.

34 Z. Li, J. Zhang and X. Lou, *Angew. Chem., Int. Ed.*, 2015, **54**, 12886–12890.

35 X. Liang and L. Nazar, *ACS Nano*, 2016, **10**, 4192–4198.

36 X. Wang, G. Li, J. Li, Y. Zhang, A. Wook, A. Yu and Z. Chen, *Energy Environ. Sci.*, 2016, **9**, 2533–2538.

37 Y. Li, D. Ye, W. Liu, B. Shi, R. Guo, H. Zhao, H. Pei, J. Xu and J. Xie, *ACS Appl. Mater. Interfaces*, 2016, **8**, 28566–28573.

38 S. Rehman, S. Guo and Y. Hou, *Adv. Mater.*, 2016, **28**, 3167–3172.

39 J. He, L. Luo, Y. Chen and A. Manthiram, *Adv. Mater.*, 2017, **29**, 1702707.

40 Y. Tao, Y. Wei, Y. Liu, J. Wang, W. Qiao, L. Ling and D. Long, *Energy Environ. Sci.*, 2016, **9**, 3230–3239.

41 Y. Wei, Z. Kong, Y. Pan, Y. Cao, D. Long, J. Wang, W. Qiao and L. Ling, *J. Mater. Chem. A*, 2018, **6**, 5899–5909.

42 H. Lin, L. Yang, X. Jiang, G. Li, T. Zhang, Q. Yao, G. Zheng and J. Lee, *Energy Environ. Sci.*, 2017, **10**, 1476–1486.

18204 | *J. Mater. Chem. A*, 2018, **6**, 18191–18205

This journal is © The Royal Society of Chemistry 2018

43 T. Lei, W. Chen, J. Huang, C. Yan, H. Sun, C. Wang, W. Zhang, Y. Li and J. Xiong, *Adv. Energy Mater.*, 2017, **7**, 1601843.

44 Z. Xiao, Z. Yang, L. Zhang, H. Pan and R. Wang, *ACS Nano*, 2017, **11**, 8488–8498.

45 J. Zheng, J. Tian, D. Wu, M. Gu, W. Xu, C. Wang, F. Cao, M. Engelhard, J. Zhang, J. Liu and J. Xiao, *Nano Lett.*, 2014, **14**, 2345–2352.

46 J. Xu, W. Zhang, Y. Chen, H. Fan, D. Su and G. Wang, *J. Mater. Chem. A*, 2018, **6**, 2797–2807.

47 X. Li, Y. Lu, Z. Hou, W. Zhang, Y. Zhu and Y. Qian, *ACS Appl. Mater. Interfaces*, 2016, **8**, 19550–19557.

48 H. Zhang, Z. Zhao, Y. Hou, Y. Tang, Y. Dong, S. Wang, X. Hu, Z. Zhang, X. Wang and J. Qiu, *J. Mater. Chem. A*, 2018, **6**, 7133–7141.

49 L. Yin, J. Liang, G. Zhou, F. Li, R. Saito and H. Cheng, *Nano Energy*, 2016, **25**, 203–210.

50 J. Song, M. Gordin, T. Xu, S. Chen, Z. Yu, H. Sohn, J. Lu, Y. Ren, Y. Duan and D. Wang, *Angew. Chem., Int. Ed.*, 2015, **54**, 4325–4329.

51 F. Sun, J. Wang, H. Chen, W. Li, W. Qiao, D. Long and L. Ling, *ACS Appl. Mater. Interfaces*, 2013, **5**, 5630–5638.

52 Y. Li, Q. Cai, L. Wang, Q. Li, X. Peng, B. Gao, K. Huo and P. Chu, *ACS Appl. Mater. Interfaces*, 2016, **8**, 23784–23792.

53 J. Huang, Z. Wang, Z. Xu, W. Chong, X. Qin, X. Wang and J. Kim, *ACS Appl. Mater. Interfaces*, 2016, **8**, 28663–28670.

54 W. Qian, Q. Gao, Z. Li, W. Tian, H. Zhang and Q. Zhang, *ACS Appl. Mater. Interfaces*, 2017, **9**, 28366–28376.

55 L. Zhang, F. Wan, X. Wang, H. Cao, X. Dai, Z. Niu, Y. Wang and J. Chen, *ACS Appl. Mater. Interfaces*, 2018, **10**, 5594–5602.

56 X. Zhang, Y. Zhong, X. Xia, Y. Xia, D. Wang, C. Zhou, W. Tang, J. Wu and J. Tu, *ACS Appl. Mater. Interfaces*, 2018, **10**, 13598–13605.

57 Y. Sun, Y. Zhao, Y. Cui, J. Zhang, G. Zhang, W. Luo and W. Zheng, *Electrochim. Acta*, 2017, **239**, 56–64.

58 J. Ye, H. Zhang, R. Yang, X. Li and L. Qi, *Small*, 2010, **6**, 296–306.

59 W. Luo, Y. Wang, L. Wang, W. Jiang, S. Chou, S. Dou, H. Liu and J. Yang, *ACS Nano*, 2016, **10**, 10524–10532.

60 Z. Zhou, L. Pan, Y. Liu, X. D. Zhu and X. Xie, *Chem. Commun.*, 2018, **54**, 4790–4793.

61 B. Ding, L. Shen, G. Xu, P. Nie and X. Zhang, *Electrochim. Acta*, 2013, **107**, 78–84.

62 H. Liu, W. Li, D. Shen, D. Zhao and G. Wang, *J. Am. Chem. Soc.*, 2015, **137**, 13161–13166.

63 T. Zegeye, C. Kuo, A. Wotango, C. Pan, H. Chen, A. Haregewoin, J. Cheng, W. Su and B. Hwang, *J. Power Sources*, 2016, **324**, 239–252.

64 C. Nan, Z. Lin, H. Liao, M. Song, Y. Li and E. Cairns, *J. Am. Chem. Soc.*, 2014, **136**, 4659–4663.

65 W. Li, F. Wang, Y. Liu, J. Wang, J. Yang, L. Zhang, A. Elzatahry, D. Al-Dahyan, Y. Xia and D. Zhao, *Nano Lett.*, 2015, **15**, 2186–2193.

66 L. Yao, X. Dong, C. Zhang, N. Hu and Y. Zhang, *J. Mater. Chem. A*, 2018, **6**, 11260–11269.

67 S. Wu, Q. Cao, M. Wang, T. Yu, H. Wang and S. Lu, *J. Mater. Chem. A*, 2018, **6**, 10891–10897.

68 J. Yao, T. Mei, Z. Cui, Z. Yu, K. Xu and X. Wang, *Chem. Eng. J.*, 2017, **330**, 644–650.

69 C. Dai, J. Lim, M. Wang, L. Hu, Y. Chen, Y. Chen, Z. Chen, H. Chen, S. Bao, B. Shen, Y. Li, G. Henkelman and M. Xu, *Adv. Funct. Mater.*, 2018, **28**, 1704443.

70 G. Li, W. Hou, S. Jiang, Y. Huang, J. Sun and J. Geng, *Nat. Commun.*, 2016, **207**, 10601.

71 J. Zhang, Y. Shi, Y. Ding, W. Zhang and G. Yu, *Nano Lett.*, 2016, **16**, 7276–7281.

This journal is © The Royal Society of Chemistry 2018

J. Mater. Chem. A, 2018, **6**, 18191–18205 | **18205**